



Supporting Information

Data–Knowledge-Dual-Driven Electrolyte Design for Fast-Charging Lithium Ion Batteries

Yi Yang, Nan Yao, Yu-Chen Gao, Xiang Chen, Yu-Xin Huang, Shuo Zhang, Han-Bing Zhu, Lei Xu, Yu-Xing Yao, Shi-Jie Yang, Zheng Liao, Zeheng Li, Xue-Fei Wen, Peng Wu, Ting-Lu Song, Jin-Hao Yao, Jiang-Kui Hu, Chong Yan, Jia-Qi Huang* and Qiang Zhang**

SUPPORTING INFORMATION

Contents

1. Experimental methods SI3
2. Supplemental Notes SI8
3. Supplemental Tables SI10
4. Supplemental Figures SI12
5. References SI45

SUPPORTING INFORMATION

1. Experimental methods

Materials and Electrolytes. The high-loading NCM811 ($\text{LiNi}_{0.8}\text{Co}_{0.1}\text{Mn}_{0.1}\text{O}_2$) and graphite foil were purchased from Beijing Li-Volt Energy Technology Co., Ltd. The areal loading of NCM811 and graphite electrodes were about 4.0 mAh cm^{-2} (areal mass loading of electrode: 21.5 mg cm^{-2} , mass percentage of active material: 94.5%) and 4.4 mAh cm^{-2} (areal mass loading of electrode: 12.93 mg cm^{-2} , mass percentage of active material: 95.7%), respectively. Graphite and NCM811 electrodes were stored in the argon-filled glovebox. Before use, the electrodes were dried at 80°C overnight and punched into disks with diameters of 13.0 (NCM811) and 15.0 mm (graphite). Thick lithium (Li) foils ($600 \mu\text{m}$) were purchased from China Energy Lithium Co., Ltd. Polyethylene (PE) separator was purchased from Asahi Kasei Technosystem Co., and the diameter of the PE separator is 19.0 mm in coin cells.

Fluoroethylene carbonate (FEC), ethylene carbonate (EC), dimethyl carbonate (DMC), 1,3-propane sultone (1,3-PS), lithium bis(fluorosulfonyl)imide (LiFSI), and lithium hexafluorophosphate (LiPF_6) were purchased from Duoduo Chem Co., Ltd. Ethyl 2,2-dimethylbutanoate (EDMB) was purchased from the Adamas Reagent Co., Ltd. Ethyl trimethylacetate (ETMA), methyl trimethylacetate (MTMA), were purchased from Meryer (Shanghai) Chemical Technology. The solvents and lithium salts were all battery-grade. Liquid carbonate-based electrolyte (abbreviation for EC/DMC) consisted of 1.0 M LiPF_6 dissolved in EC: DMC (3:7 by volume) was prepared in an Ar-filled glove box with O_2 and H_2O content below 0.1 ppm.

The electrolytes used in LSV tests are composed of 1.0 M LiPF_6 dissolved in a single solvent, including EC, DMC, MTMA, ETMA, and EDMB. Electrolytes of carboxylate-based ETMA/MTMA/EDMB electrolytes were prepared by dissolving a specific amount of 1.5 M LiFSI into corresponding carboxylate/FEC mixture solvents (9:1 [v/v]), followed by stirring at room temperature. Then, 1% 1,3-PS (by weight) was added into the LiFSI corresponding carboxylate/FEC mixture electrolyte. All electrolytes were prepared and stored in an argon-filled glovebox (Mikrouna; oxygen, < 0.1 ppm; water, < 0.1 ppm) at room temperature.

Cell Assembly. The graphite||NCM811 full cells were assembled in standard 2032 coin-type cells with 50 μL electrolyte in an Ar-filled glove box with both oxygen and water contents below 0.1 ppm. All the coin cells were allowed to stand for 10 hours before pre-cycle to soak the electrodes.

Dry graphite (areal mass loading of electrode: 7.32 mg cm^{-2} , mass percentage of active material: 97.0%)||NCM811 (areal mass loading of electrode: 11.14 mg cm^{-2} , mass percentage of active material: 95.2%) pouch cells (no electrolyte injection) were provided by LiFUND Technology (Zhuzhou City, Hunan Province, China). Cells were dried and vacuum sealed before shipping to Tsinghua University, where they were cut open, injected with electrolyte (0.9 mL), and vacuum sealed at -70 kPa in a dry room with a dew point below -50°C . Next, cells were rested for 10 h to ensure complete electrode wetting, after 2 formation cycles at 0.05 C, degassed, and vacuum sealed again at -85 kPa .

Electrochemical Measurements. The pre-cycle and cell tests were conducted on the LAND battery cycler (Wuhan LAND Electronic Co. Ltd.) and Neware battery test system (MIHW-200-160CH, Neware Technology, Shenzhen, China). Each cell underwent 2 formation cycles (0.05C-rate) before additional testing. The

SUPPORTING INFORMATION

theoretical capacity was used to set the C-rates and the de-intercalation capacity. For graphite||NCM811 batteries, the formation and subsequent cycles of coin cells were scanned between 2.8 and 4.3 V.

The oxidative stability of the electrolytes was evaluated via LSV test of coin-type Li||Al@C (carbon coated Al) cells between 3.0 and 6.0 V at 0.1 mV s⁻¹ under 25°C. The potentiostatic floating tests were conducted by Li||NCM811 cells maintained at 4.3–4.7 V for a period of 5 h after being charged to 4.3 V at 0.05 C. The Li||Cu half cells were tested under 1 mA cm⁻² and 1 mAh cm⁻². The test magnifications of the graphite||NCM811 full cells at 25°C, 45°C and 60°C were 1.0, 0.5, and 0.2 C, respectively, but the cells with MTMA-based electrolytes only cycled with ≤ 0.2 C at 45°C. The graphite||NCM811 full cell employing ETMA-based electrolyte cycled at 100°C and 0.2 C. The low-temperature discharge performance of graphite||NCM811 full cells at -20°C and -30°C were conducted under 0.1 and 0.05 C, respectively. The EIS test of graphite||NCM811 full cells (two electrodes test) under 45°C was carried out at a voltage amplitude of 10 mV and in a frequency range of 10⁵–10⁻¹ Hz, conducted on a Solartron 1470E electrochemical workstation, after per cycles under 1.0 C. Temperature-dependent EIS measurements of Li||Li-reference||graphite three electrodes coin-type half-cells were carried out at a voltage amplitude of 10 mV and in a frequency range of 10⁵–10⁻¹ Hz under varied temperature (-10°C, 0°C, 10°C, 20°C, and 30°C). Li||Li-reference||graphite three electrodes half-cells were charged to 50% SOC (state of charge) at 0.05 C after 2 formation cycles at 0.05 C in the voltage range of 0.001–1.5 V and 25°C before EIS measurements. The Li⁺ desolvation activation energies were obtained by fitting EIS spectra according to the Arrhenius Equation:

$$k = Ae^{\frac{-E_a}{RT}} \quad (S1)$$

where k is the rate constant, A the pre-exponential factor, R the idea gas constant, T the temperature in kelvin, and E_a the Li⁺ de-solvation activation energy. DRT analysis of the data was performed using the pyDRTtools software proposed by Ciucci et al., which is publicly available on GitHub: <https://github.com/ciuccislab/pyDRTtools>. The low-temperature performance of pouch cells was tested at -20°C and 0.05 C, -30°C and 0.05 C, -40°C and 0.05 C, -50°C and 0.025 C, and -60°C and 0.006 C, respectively.

Characterization. The cycled Li||graphite and graphite||NCM811 cells were disassembled in the Ar-filled glovebox, and graphite electrodes were recollected followed by washing three times with DMC solvents to remove the residual electrolyte. Cryo-TEM images were obtained using a JEOL 2100plus TEM with the assistance of a cryo-transfer holder (Gatan 698) to detect the SEI on graphite electrodes. After fetching and washing the samples in the glovebox, the samples were transferred to the cryo-transfer holder in an atmosphere of liquid nitrogen cryogen. Then, the holder was transferred into the TEM, followed by freezing and stabilizing the samples to about -170°C. ToF-SIMs (PHI nano ToF II, ULVAC-PHI) were used to investigate SEI components on graphite anodes. A special transfer vessel, which can directly transfer the sample from the glovebox to the vacuum chamber of ToF-SIMs, was used during sample transfer without being exposed to ambient air. The sputter etching was performed using an Ar⁺ beam (3 kV 100 nA) to obtain a depth profile. The area of analysis is 50 μm × 50 μm, while the sputtering area is 400 μm × 400 μm. Meanwhile, XPS (Kratos Analytical, Axis Supra+) was conducted to investigate the SEI components on graphite anodes. The

SUPPORTING INFORMATION

depth profiles were acquired via Ar⁺ sputtering at 2 kV for 0, 15, 30, and 45 s. Graphite electrodes cycled at high temperatures were characterized by SEM at 5.0 kV (FEI-APREO, Thermo Fisher Scientific). The thermal behaviors of pouch cells were tested by a standard accelerating rate calorimeter (ARC, Thermal Hazard Technology). The range of testing temperature was set at 50.0–300.0°C. The limit for detecting the self-heating rate was 0.02°C min⁻¹. One internal and two external thermocouples with a high acquisition frequency of 10 Hz were used to ensure a high accuracy of the obtained temperature.

Molecular Generation. The generation of molecular structures utilized the Surge tool^[1], creating a database of molecules containing no more than 10 heavy atoms and consisting solely of carbon, hydrogen, and oxygen elements. During the generation process, molecules were designed to comply with Bredt's rule, and only planar graphs were produced since non-planar graphs cannot be converted to practical molecules. After that, molecules containing functional groups such as hydroxyl or carboxyl groups, where active hydrogens are reactive with active materials in the battery, were excluded from the database.

High-throughput Calculation. The high-throughput calculation consists of eight-round tasks including both density functional theory (DFT) calculations and molecular dynamics (MD) simulations:

- 1) Optimizing the geometric structure of a molecule in a vacuum by DFT calculations;
- 2) Calculating the solvation parameters of solvents by MD simulations using the Charge Model 1A (CM1A) charge;
- 3) Optimizing the geometric structure of a molecule in a solvent environment using CM1A-based parameters by DFT calculations;
- 4) Calculating the solvation parameters of solvents by MD simulations using the advanced restrained electrostatic potential (RESP2) charge;
- 5) Optimizing the geometric structure and then calculating the properties of a molecule in a solvent environment using RESP2-based parameters by DFT calculations;
- 6) Optimizing the geometric structure and then calculating the properties of a Li⁺ in a solvent environment using RESP2-based parameters by DFT calculations;
- 7) Optimizing the geometric structure and then calculating the properties of a Li⁺–molecule cluster in a solvent environment using RESP2-based parameters by DFT calculations;
- 8) Calculating the solvation structure and physicochemical properties of an electrolyte consisting of the molecule and around 1.0 M LiFSI salt by MD simulations.

Density Functional Theory Calculations. Structures of molecules and ion–molecule (ion = Li⁺ or Mn²⁺) complexes were optimized by Gaussian 16 with the Becke's three-parameter hybrid method using the Lee–Yang–Parr correlation (B3LYP) functional at a basis set of 6-311+G(d, p).^[2, 3] The solvation effect was considered with the SMD model using the parameters of the molecules themselves, where the dielectric constants were calculated by MD simulations. Multiple ion–molecule binding structures were constructed for each molecule, and the most stable one, i.e., the one with the lowest energy, was determined as the final

SUPPORTING INFORMATION

structure. Frequency analysis was performed to ensure the ground state of optimized structures. The binding energy between an ion and a molecule was defined as follows:

$$E_b = E_{\text{ion-molecule}} - E_{\text{ion}} - E_{\text{molecule}} \quad (\text{S2})$$

where $E_{\text{ion-molecule}}$, E_{ion} , and E_{molecule} represent the energy of the ion–molecule complex, ion, and molecule, respectively.

Molecular Dynamics Simulations. MD simulations were conducted using the Large Scale Atomic/Molecular Massively Parallel Simulator (LAMMPS) code and the Optimized Potential for Liquid Simulations-all atom (OPLS-AA) force field.^[4, 5, 6] Each model contains 200 molecules. Electrolyte models contain another 20 LiFSI molecules. The CM1A parameters were generated by the LigParGen while RESP2 atomic partial charges were obtained based on electrostatic potential (ESP) charges from DFT calculations in both vacuum and solvent environments using the Multiwfn program.^[7, 8, 9, 10, 11] The parameters of Li^+ and FSI^- were obtained from Jensen *et al.*^[12] and Lopes *et al.*, respectively.^[13] The initial atomic coordinates were generated with the Packing Optimization for Molecular Dynamics Simulations (PACKMOL)^[14] program. The periodic boundary conditions (PBCs) were applied in all three directions for all simulations. A cutoff of 12 Å was used for both van der Waals interactions and long-range correction (particle–particle particle-mesh) of Coulombic interactions. The time step was fixed to be 1 fs. All models were first relaxed in an NVT ensemble under the Nose–Hoover thermostat for 0.5 ns to maintain a temperature of 298 K with a time constant of 0.1 ps^[15, 16], and then equilibrated in an NPT ensemble for 1 ns at 298 K and a pressure of 1 atm with a time constant of 1 ps using the Parrinello–Rahman barostat.^[17] After that, the systems were heated from 298 to 400 K within 0.5 ns, and maintained at 400 K for 0.5 ns, followed by being annealed from 400 to 298 K within 0.5 ns and equilibrated at 298 K for another 1 ns. A 20 ns production run was finally conducted in an NVT ensemble, which was used for determining the dielectric constant by the method reported in the literature.^[18, 19]

Solvation structures of the EC/DMC- and ETMA-based electrolytes were also analyzed by MD simulations running at 318 K. The EC/DMC-based model contains 540 EC, 992 DMC, and 120 LiPF_6 molecules, while the ETMA-based model contains 705 ETMA, 168 FEC and 180 LiFSI molecules. The parameters of PF_6^- was obtained from Doherty *et al.*^[20]

Molecular Property Prediction. The Uni-Mol model^[21] served as a versatile platform for predicting molecular properties. For properties such as melting and boiling, databases from PubChem,^[22] ChemSpider,^[23] and AAT Bioquest were utilized, with individual models established for each property. Other properties were derived from DFT and MD calculations, using a single unified model for their prediction. SMILES^[24] and property databases were used as inputs to fine-tune the Uni-Mol model and molecules from a self-constructed structural database were inferred.

Clustering Analysis. Each molecule was represented as a 2048-dimensional vector by the Extended Connectivity Circular Fingerprints (ECFPs) with a radius of 2.^[25] All molecular fingerprints were then used for

SUPPORTING INFORMATION

clustering analysis based on the t-distributed stochastic neighbor embedding (t-SNE) algorithm by the Python package scikit-learn^[26, 27].

SUPPORTING INFORMATION

2. Supplemental Notes**2.1. Note S1.** High-temperature performance of the cells employing screened solvents-based electrolytes

The electrochemical performances of four electrolytes under variant conditions (45°C, and 60°C) were evaluated in graphite||NCM811 (4.0 mAh cm⁻²) cells. Under 45°C, the screened-out ETMA and EDMB molecules afforded the cell with a discharge capacity larger than 3.3 mAh cm⁻² after 100 cycles at 0.5 C (Figure S7A). However, the cell using MTMA-based electrolyte only underwent 10 cycles at 45°C with 0.2 C rate (Figure S7B). Even more, the cells using ETMA and EDMB electrolytes can be steadily cycled under 60°C and 0.2 C with only 5.0% and 6.5% capacity degradation respectively, after 35 cycles, while the EC/DMC-based electrolyte can hardly work under the same condition (Figure S8). To further explore the limit of high-temperature performances, the ETMA-based cell was tested under 100°C and 0.2 C (Figure S9). Despite a quick capacity degradation, the cell can operate reliably without the risk of explosion, which is a rarely-observed characteristic in other carboxylate electrolytes. Therefore, only ETMA and EDMB satisfy the requirement of working at high temperatures.

2.2. Note S2. Low-temperature performance of cells with ETMA- and EC/DMC-based electrolytes

At -20°C, the ETMA-based electrolyte possesses good fluidity, while the routine EC/DMC-based electrolyte is almost frozen (Figure S12). When cycling under -20°C at 0.1 C, the discharge capacity of the cell using the EC/DMC electrolyte dropped to almost 0 due to the electrolyte solidification (Figure S13). Conversely, the cells employing ETMA-based electrolytes and electrodes having a high loading of active materials can achieve discharge capacities over 3.0 mAh cm⁻² and 1.8 mAh cm⁻² under -20°C at 0.1 C and under -30°C at 0.05 C, respectively, suggesting the outstanding performance of the ETMA-based electrolyte at low temperatures (Figure S14).

2.3. Note S3. Solvation structures in ETMA- and EC/DMC-based electrolyte

For the EC/DMC-based electrolyte, the solvation sheaths of Li⁺ are mainly composed of EC and DMC molecules, and only a few PF₆⁻ anions are involved (Figure S15). Specifically, 44.1% and 46.6% Li⁺ ions are coordinated with zero and only one PF₆⁻, respectively (Figure S16A). In contrast, much more FSI⁻ anions and FEC molecules participate in Li⁺ solvation structures than solvent molecules in the ETMA-based electrolyte as indicated by the distinct Li-O_{FSI}⁻ peak at about 2.1 Å (Figure S16B and Figure S17). The solvation sheaths with 1, 2, 3, and 4 FSI⁻ account for 24.9%, 57.6%, 13.0%, and 2.8%, respectively. The anion-rich Li⁺ solvation structure can be attributed to the significant steric effect caused by the three methyl groups in ETMA, which weakens the interaction between Li⁺ and ETMA.

2.4. Note S4. SEI analysis by ToF-SIMS

The ionic fragments of organic components (C₂H₃O⁻)^[28], which are mainly decomposed from solvents, are detected priorly at the top surface of the SEI of both electrolytes, beneath are the LiF inorganic constituents (LiF⁻)^[29]. Differently, the SEI generated in the EC/DMC-based electrolyte contains more organic components than that in the ETMA-based electrolyte, suggesting more solvent molecules involved in the formation of SEI

SUPPORTING INFORMATION

in the EC/DMC-based electrolyte (Figure S18). The depth profiles reflecting the three-dimensional (3D) structure of SEI and spatial distribution of organic/inorganic components were further obtained from ToF-SIMS. With the increasing sputtering time, the intensities of LiF in both SEIs remain high, but the SEI in the ETMA-based electrolyte is distinctly LiF richer than that in the EC/DMC-based electrolyte (Figure S19A). The content of organic components in the SEI derived from the ETMA-based electrolyte is about 4 times lower than that in the EC/DMC-based electrolyte (Figure S19B). Meanwhile, the SO_2^- and Li_3N^- fragments in the top layer of SEI formed in the ETMA-based electrolyte are evident (Figure S23).

2.5. Note S5. Low-temperature performance of Li-ion pouch cells with ETMA-based electrolyte

The graphite||NCM811 pouch cells also exhibited exceptional performance at low temperatures (Figure S32), leveraging from the low melting point of ETMA. The cells employing the ETMA-based electrolyte can deliver a capacity retention of 85% at -20°C , 78% at -30°C , 71% at -40°C , 58% at -50°C , 54% at -60°C , with corresponding energy density of 143.4, 122.0, 98.7, 76.0, 68.2 Wh kg^{-1} , respectively.

SUPPORTING INFORMATION

3. Supplemental Tables

Table S1. The 35 molecules with binding energy of Mn²⁺ (Mn BE) > -2 eV.

SMILES	CAS number	Mn BE (eV)
<chem>CCCC(=O)OC</chem>	623-42-7	-0.98337
<chem>CCC(C)OC(C)=O</chem>	105-46-4	-0.93118
<chem>CCOC(=O)C(C)C</chem>	97-62-1	-1.1179
<chem>CC(=O)OCC(C)C</chem>	110-19-0	-0.7907
<chem>CCCCOC(C)=O</chem>	123-86-4	-0.87839
<chem>COC(=O)C(C)(C)C</chem>	598-98-1	-0.867
<chem>CCC1COC(=O)C1</chem>	16496-51-8	0.001524
<chem>CCC(CC)C(=O)OC</chem>	816-11-5	-0.95782
<chem>CCC(C)(C)C(=O)OC</chem>	813-67-2	-1.02125
<chem>CCOC(=O)C(C)(C)C</chem>	3938-95-2	-1.7742
<chem>CC(=O)OC(C)C(C)C</chem>	5343-96-4	-1.83259
<chem>CCCC(C)C(=O)OC</chem>	2177-77-7	-1.25566
<chem>CCOC(=O)C(C)CC</chem>	7452-79-1	-1.7166
<chem>CCCC(=O)OC(C)C</chem>	638-11-9	-1.7361
<chem>CCCCCOC(C)=O</chem>	628-63-7	-1.57377
<chem>CCCC(C)OC(C)=O</chem>	626-38-0	-1.78206
<chem>CCC(C)COC(C)=O</chem>	624-41-9	-1.0239
<chem>CCCCOC(=O)CC</chem>	590-01-2	-1.78492
<chem>CCCOC(=O)C(C)C</chem>	644-49-5	-1.4161
<chem>CC(=O)OC1CCCC1</chem>	933-05-1	-0.8418
<chem>CCCOC(=O)C(C)CC</chem>	37064-20-3	-1.2788
<chem>CC(=O)OC1CCCC1C</chem>	NONE	-1.85589
<chem>CCC(C)C(=O)OC(C)C</chem>	66576-71-4	-1.8227
<chem>CCCOC(=O)C(C)(C)C</chem>	5129-35-1	-1.38102
<chem>CC(C)C(=O)OC(C)(C)C</chem>	16889-72-8	-1.4812
<chem>CCC(=O)OC(C)(C)CC</chem>	34949-22-9	-1.45805

SUPPORTING INFORMATION

CCCC(C)(C)OC(C)=O	34859-98-8	-1.61823
COC(=O)C(C)CC(C)C	71672-33-8	-1.60417
CCC(=O)OC(CC)CC	5468-56-4	-1.68291
CC(C)COC(=O)C(C)C	97-85-8	-1.453
CCCCOC(=O)C(C)C	97-87-0	-1.72
CC(C)OC(=O)C(C)(C)C	5129-36-2	-1.80062
CCOC(=O)C(C)(C)CC	5129-40-8	-1.0816
CCCC(C)COC(C)=O	7789-99-3	-1.9995
CCC(C)OC(=O)C(C)C	23412-21-7	-1.77319

Table S2. Comparison of R_{CEI} and R_{SEI} in cells using two electrolytes cycled 45°C.

Cycle number	EC/DMC-based	ETMA-based
	$R_{\text{CEI}} (\Omega)$	$R_{\text{CEI}} (\Omega)$
5	2.7	24.2
25	8.2	24.9
50	10.4	25.8

SUPPORTING INFORMATION

4. Supplemental Figures

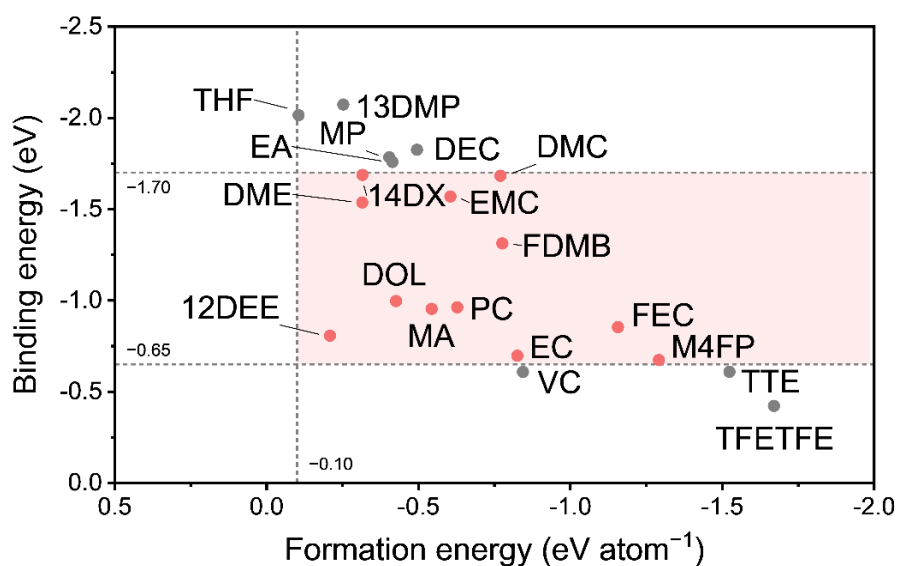


Figure S1. Formation energies of common molecules used in lithium-ion battery electrolytes. THF (tetrahydrofuran), 13DMP (1,3-dimethoxypropane), EA (ethyl acetate), MP (methyl propionate), DEC (diethyl carbonate), DMC (dimethyl carbonate), DME (1,2-dimethoxyethane), 14DX (1,4-dioxane), EMC (ethyl methyl carbonate), FDMB (fluorinated 1,4-dimethoxybutane), DOL (1,3-dioxolane), MA (methyl acetate), PC (propylene carbonate), FEC (fluoroethylene carbonate), 12DEE (1,2-diethoxyethane), EC (ethylene carbonate), M4FP (methyl 2,3,3,3-tetrafluoro propionate), VC (vinylene carbonate), TTE (1,1,2,2-tetrafluoroethyl-2,2,3,3-tetrafluoropropylether), TFETFE (1,1'-[(1,1,2,2-tetrafluoroethylene)bis(oxy)]bis[1,2,2-trifluoroethylene]).

SUPPORTING INFORMATION

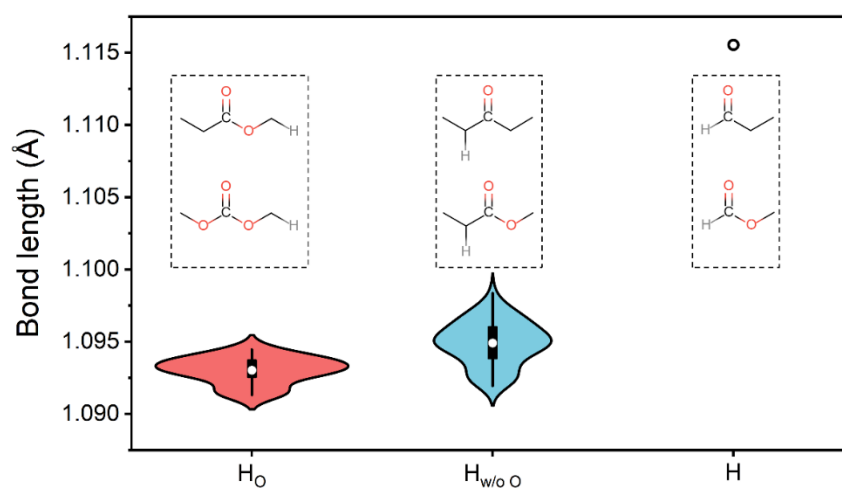


Figure S2. Violin plots of bond length data grouped by H types. The outer shells of the violins bound all data, narrow vertical lines bound 95% of the data, thick vertical lines bound 50% of the data, and white circles represent average values.

SUPPORTING INFORMATION

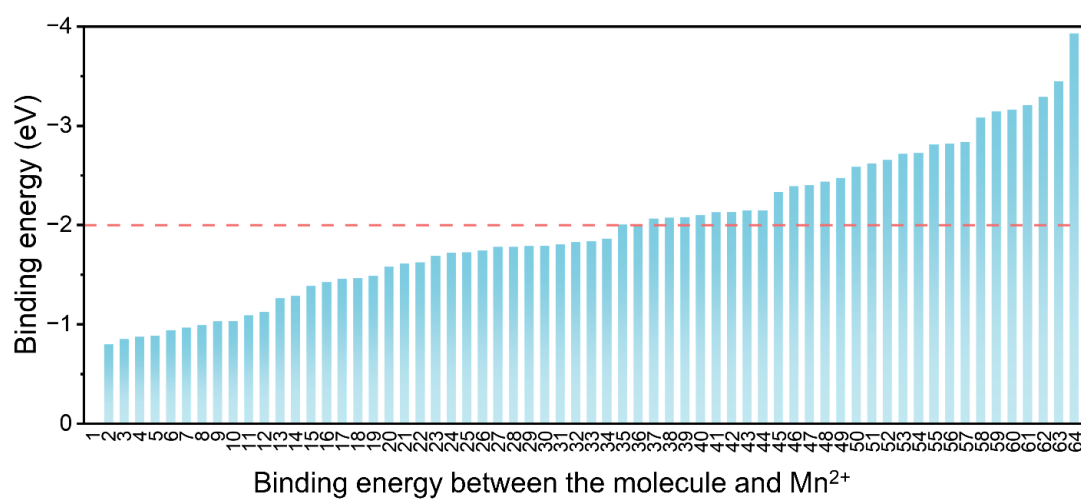


Figure S3. Binding energy of 64 molecules with Mn²⁺ which are screened after the step of chemical stability.

SUPPORTING INFORMATION

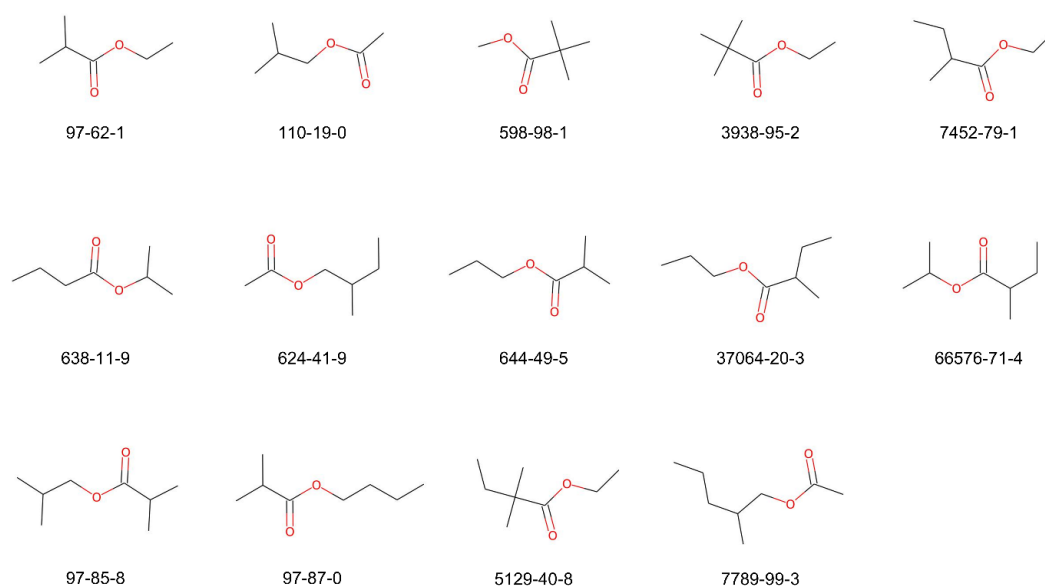


Figure S4. 14 molecules screened out by the data-knowledge-dual-driven screening step. Below each molecule is the corresponding CAS number.

SUPPORTING INFORMATION

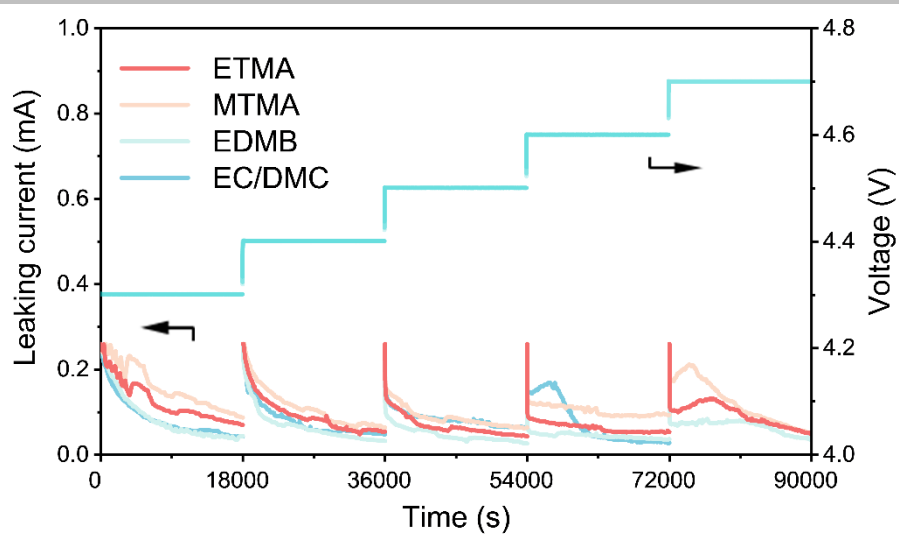


Figure S5. Potentiostatic floating profiles Li||NCM811 cells maintained at 4.3–4.7 V for a period of 5 h.

SUPPORTING INFORMATION

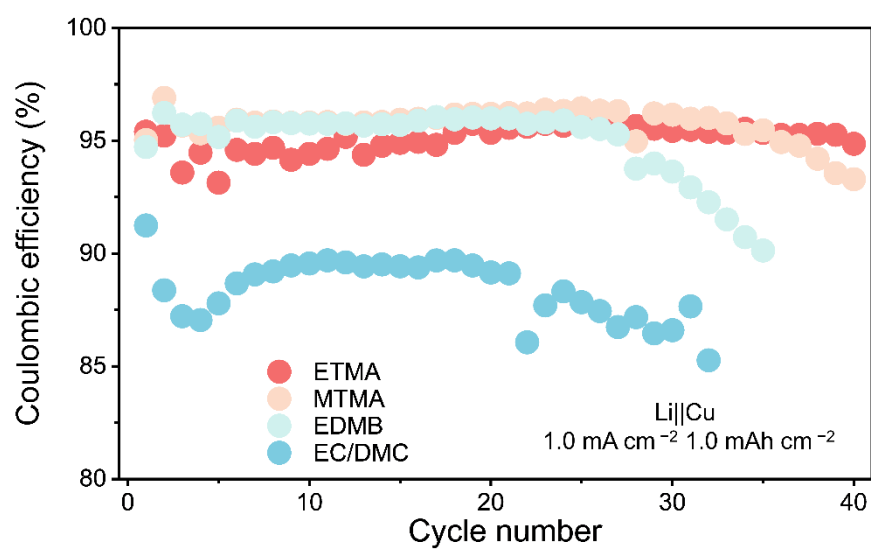


Figure S6. The performance of Li||Cu half cells using different electrolytes under 1.0 mA cm^{-2} and 1.0 mAh cm^{-2} .

SUPPORTING INFORMATION

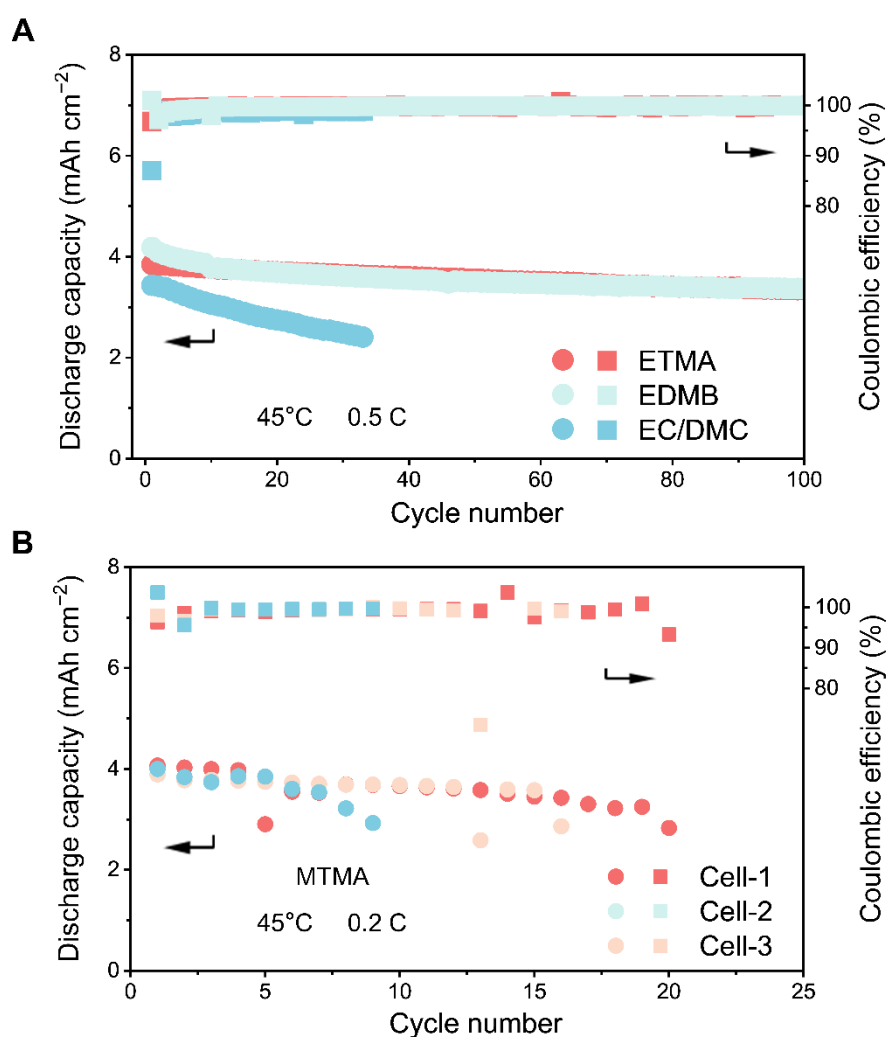


Figure S7. Cycling performance of cells employing different electrolytes under 45°C. (A) The graphite||NCM811 full cells employing ETMA-, EDMB- and EC/DMC-based electrolytes under 45°C and 0.5 C. (B) The graphite||NCM811 full cells using MTMA-based electrolytes under 45°C and 0.2 C.

SUPPORTING INFORMATION

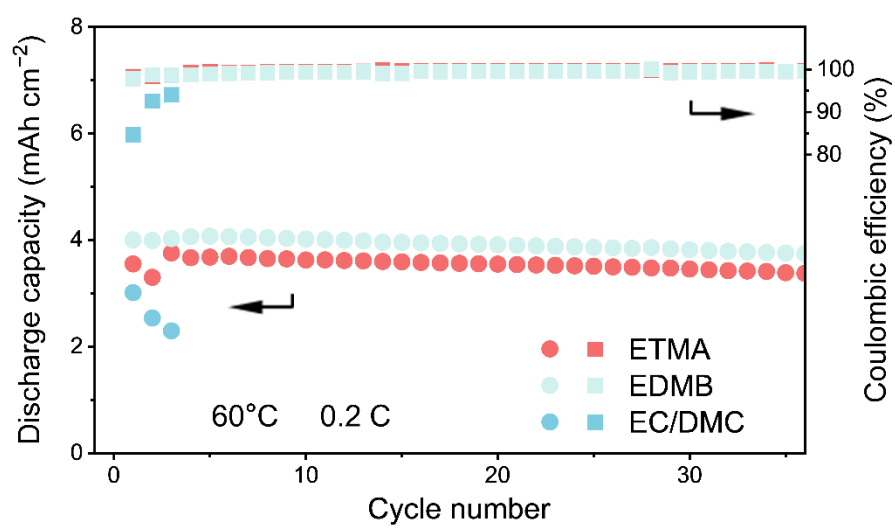


Figure S8. The performance of graphite||NCM811 full cells using different electrolytes under 60°C and 0.2 C.

SUPPORTING INFORMATION

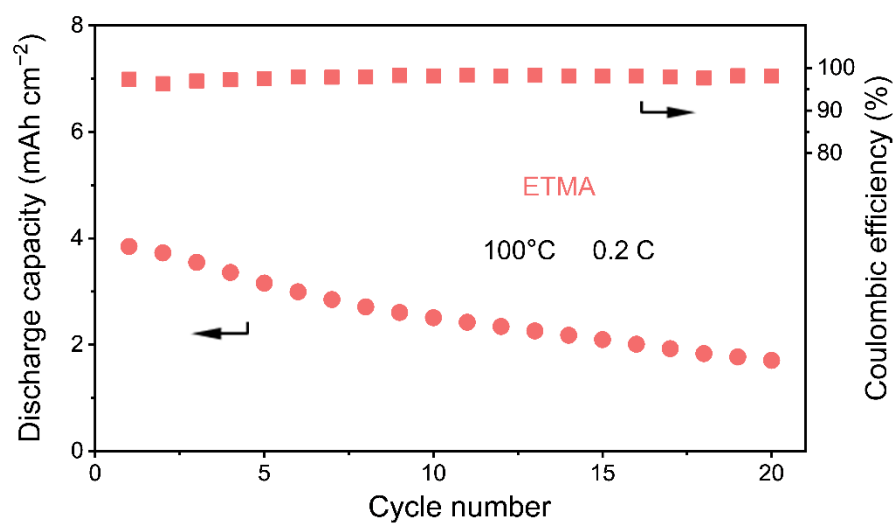


Figure S9. The performance of graphite||NCM811 full cells using ETMA-based electrolytes under 100°C and 0.2 C.

SUPPORTING INFORMATION

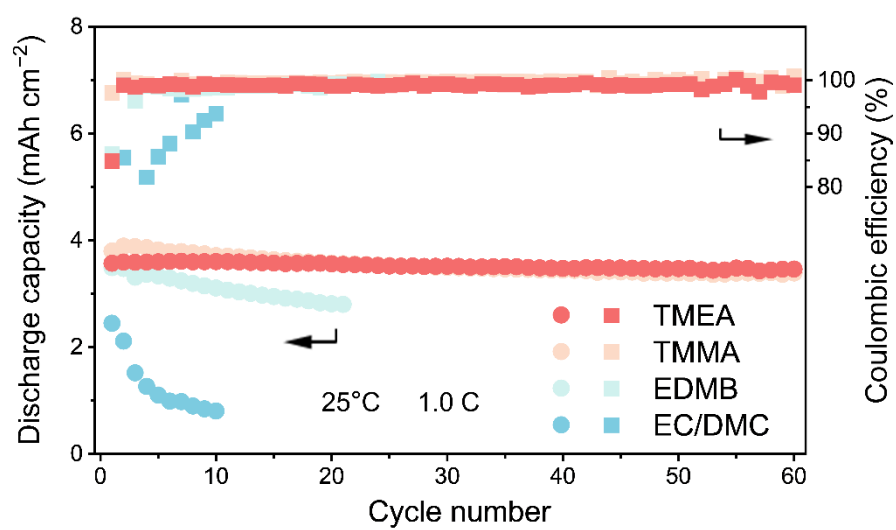


Figure S10. Cycling performance of the graphite||NCM811 full cells employing different electrolytes under 25°C and 1.0 C

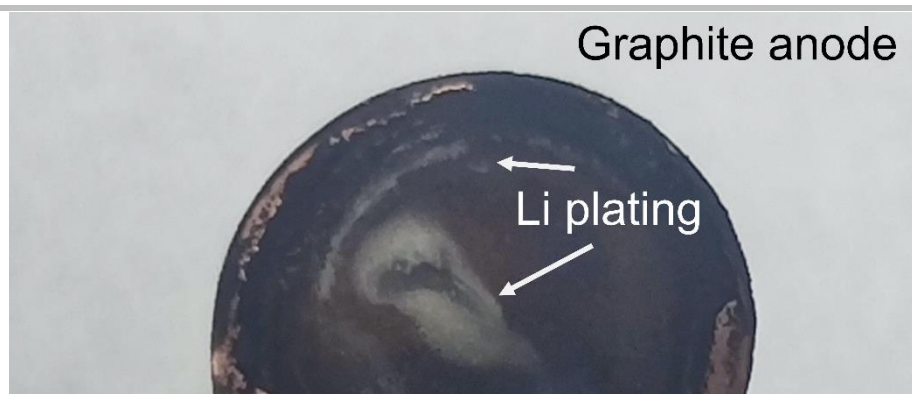


Figure S11. The optical image of cycled graphite anode with Li plating in EC/DMC-based electrolytes.

SUPPORTING INFORMATION

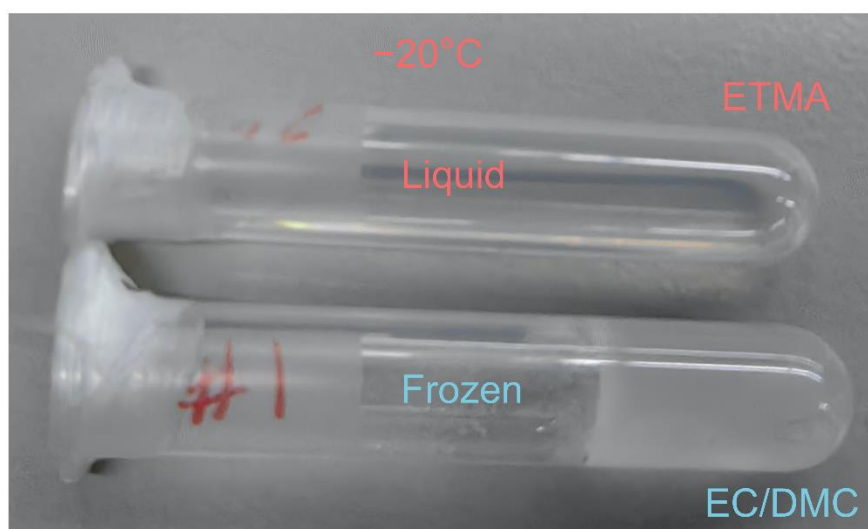


Figure S12. The photo of EC/DMC- and ETMA-based electrolytes under -20°C .

SUPPORTING INFORMATION

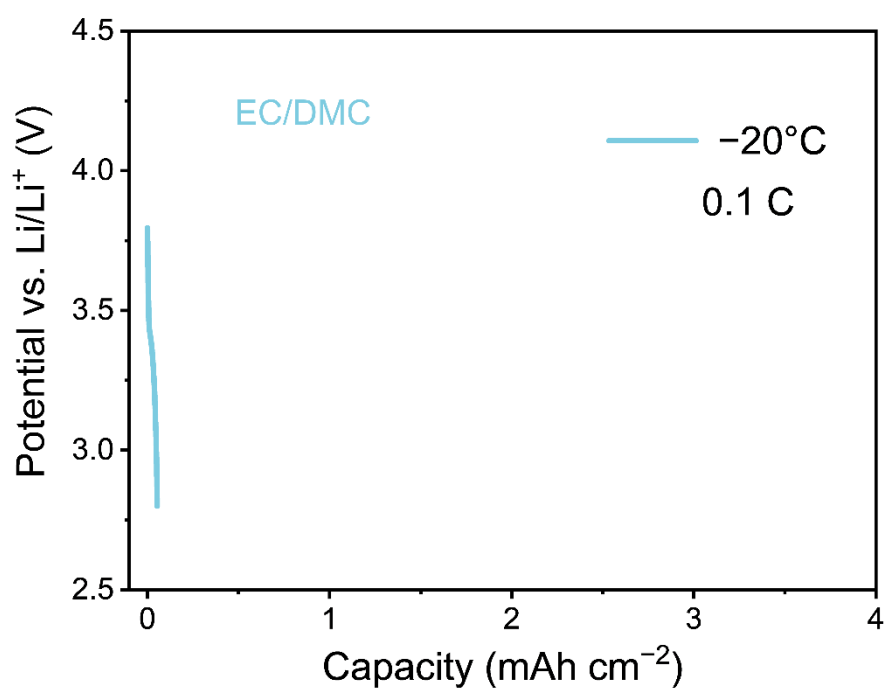


Figure S13. The discharge curve of graphite||NCM811 full cells using EC/DMC-based electrolytes under -20°C and 0.1 C.

SUPPORTING INFORMATION

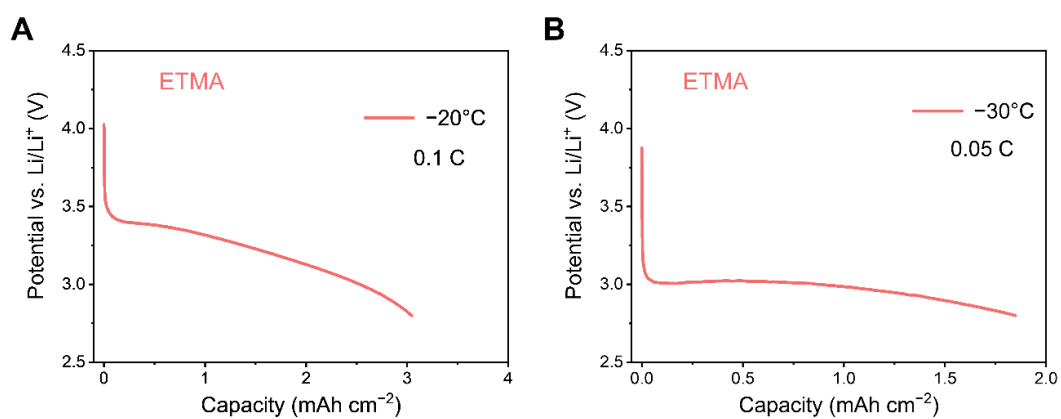


Figure S14. Discharge performance of cells under low temperatures. (A and B) The discharge curve of graphite||NCM811 full cells using ETMA-based electrolytes under -20°C (A) and -30°C (B) with 0.1 and 0.05 C, respectively.

SUPPORTING INFORMATION

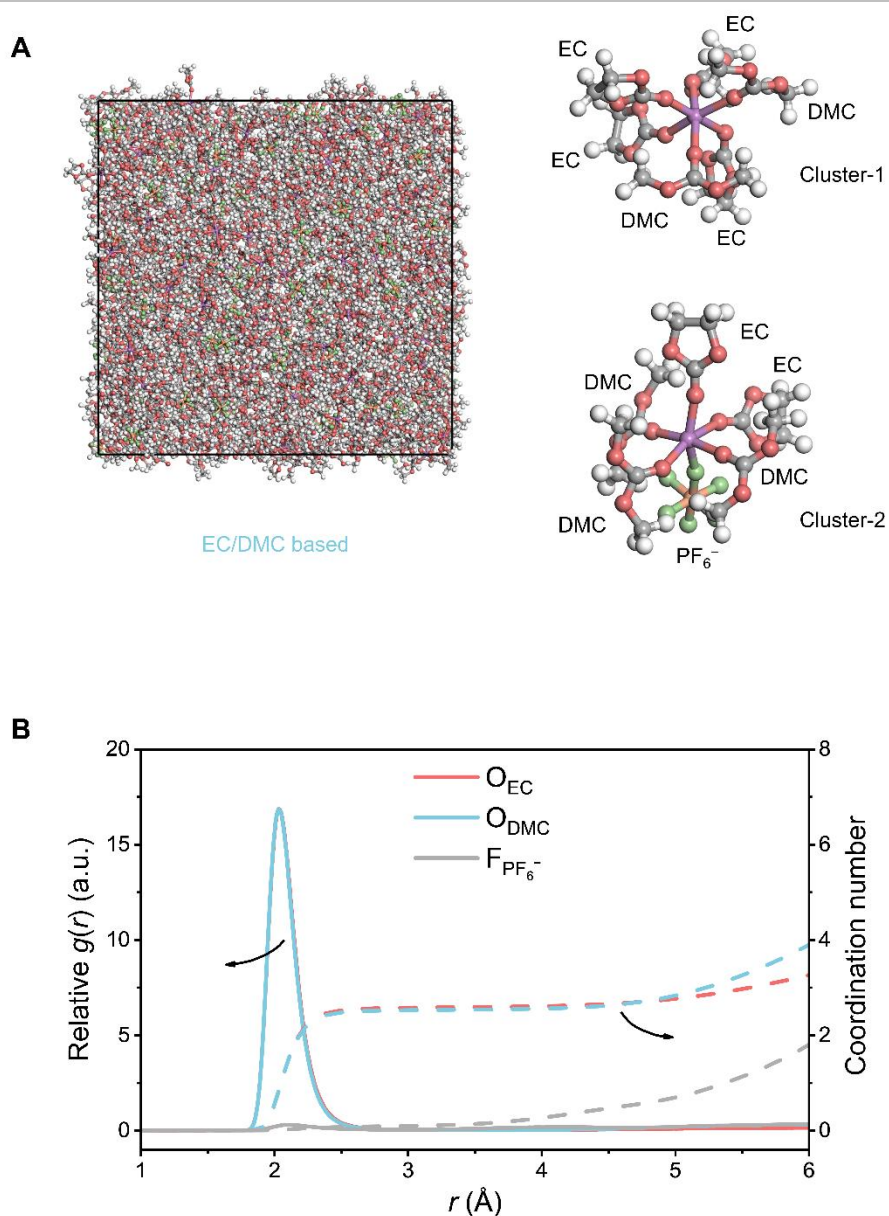


Figure S15. Solvation structure analyses of the EC/DMC-based electrolyte obtained from MD simulations. (A) The snapshot of the MD simulation box and typical solvation structures of Li^+ . (B) Radial distribution function of different species around Li^+ . Colors of elements: H-white, Li-purple, C-gray, O-red, P-orange, and F-green.

SUPPORTING INFORMATION

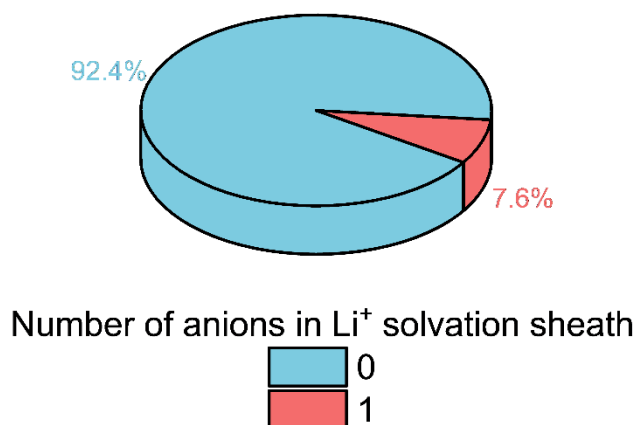
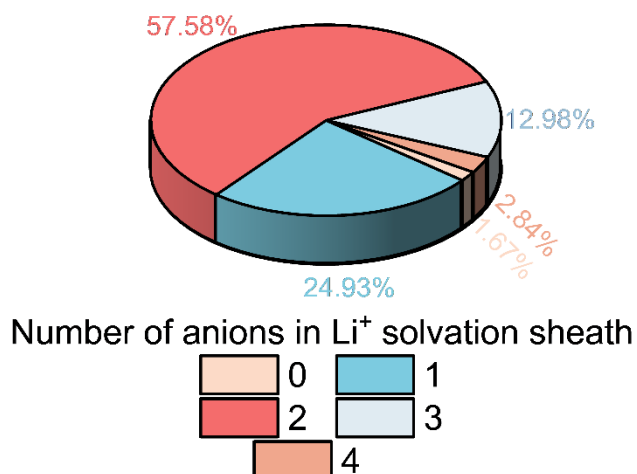
A EC/DMC based**B** ETMA based

Figure S16. The number of anions in Li⁺ solvation sheath. (A and B) The proportion of anions in Li⁺ solvation structure in EC/DMC- (A) and ETMA- (B) based electrolyte. Only 7.6% anions participate in the Li⁺ solvation sheath, whereas more than 98.33% proportion of anions enter the Li⁺ solvated structure in ETMA-based electrolytes.

SUPPORTING INFORMATION

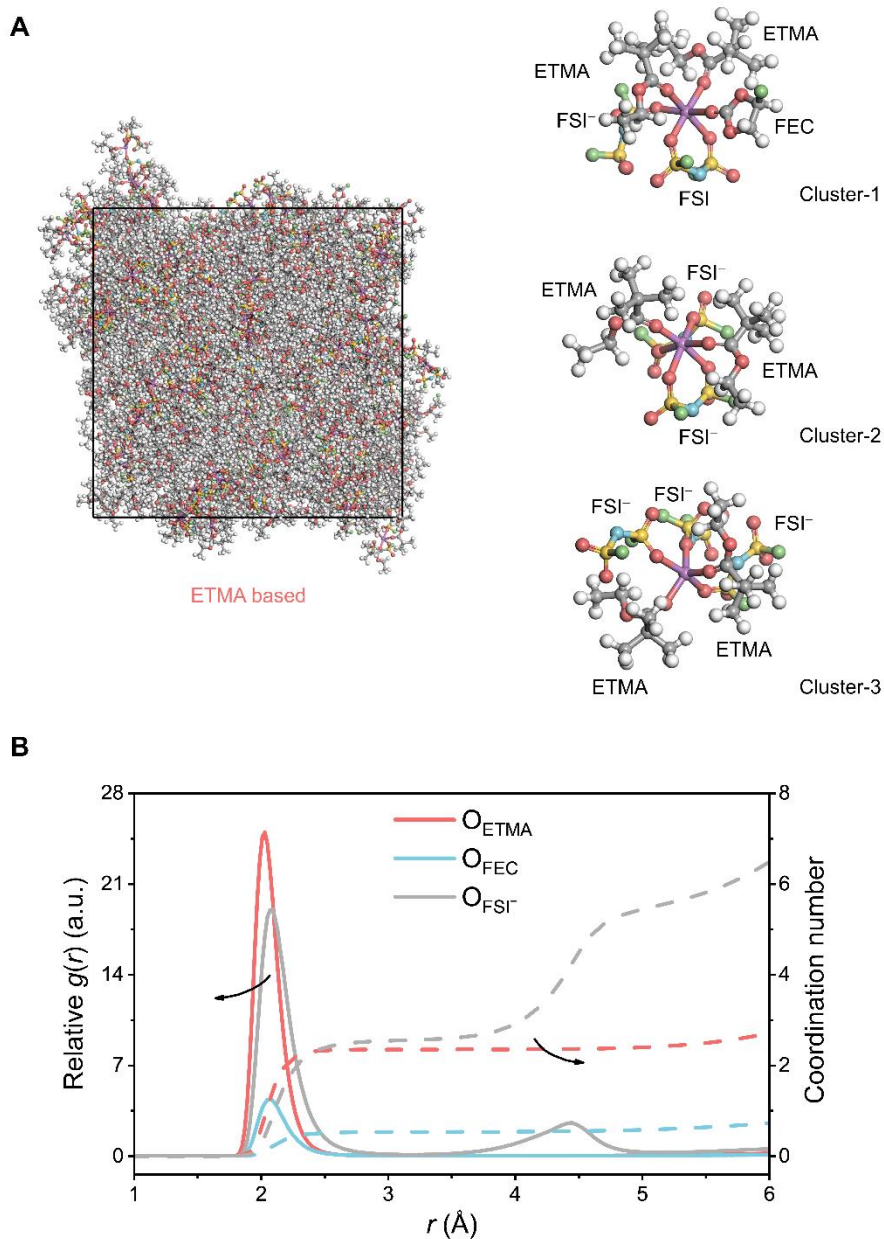


Figure S17. Solvation structure analyses of the ETMA-based electrolyte obtained from MD simulations. (A) The snapshot of the MD simulation box and typical solvation structures of Li^+ . (B) Radial distribution function of different species around Li^+ . Colors of elements: H-white, Li-purple, C-gray, O-red, N-blue, F-argent, and S-yellow.

SUPPORTING INFORMATION

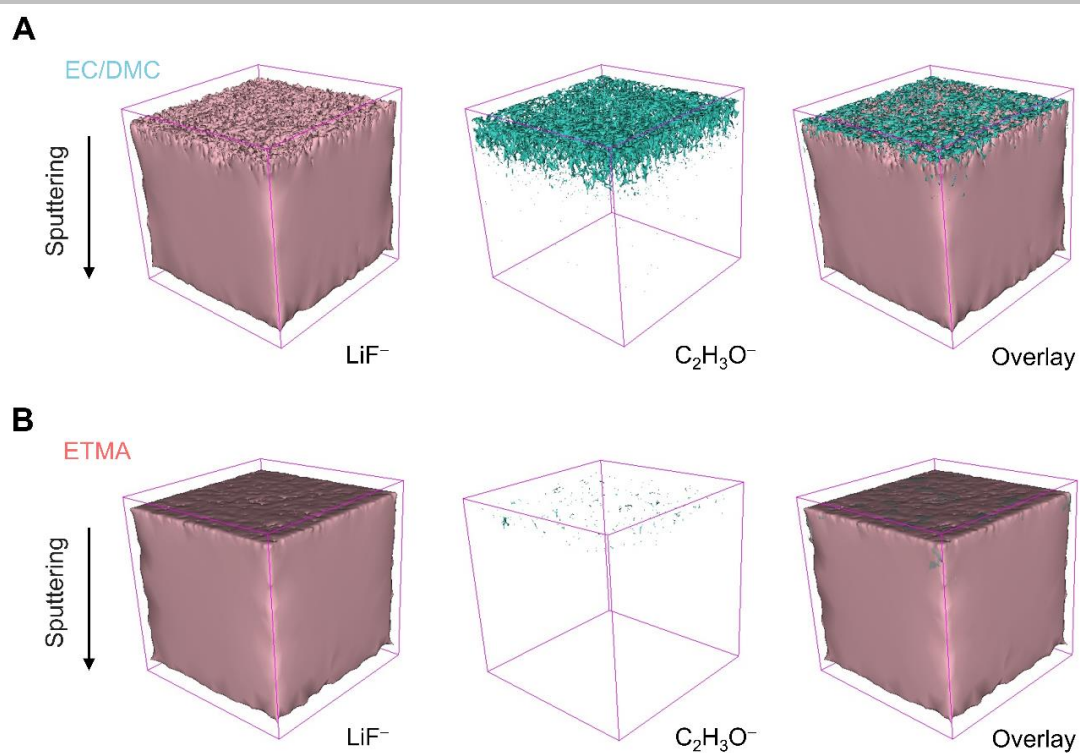


Figure S18. The 3D nanostructure of SEI resolved by ToF-SIMs. (A and B) The 3D reconstruction of LiF^- (for LiF) and $\text{C}_2\text{H}_3\text{O}^-$ (for organic components) in the ToF-SIMs sputtered volumes of SEI formed in EC/DMC-based electrolyte (A) and ETMA-based electrolyte (B).

SUPPORTING INFORMATION

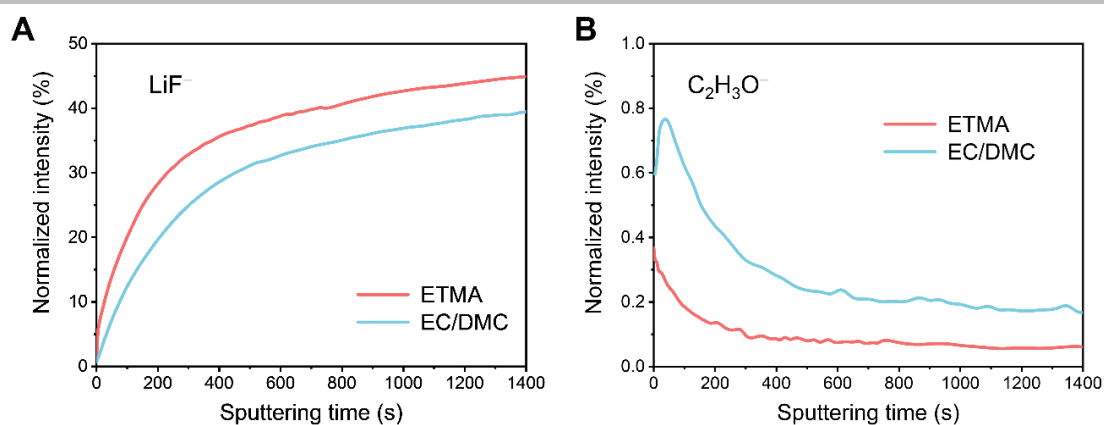


Figure S19. The depth profiles of SEI resolved by ToF-SIMS. (A and B) The corresponding ToF-SIMS depth profiles for LiF^- (A) and $\text{C}_2\text{H}_3\text{O}^-$ (B) in different SEIs. Normalized intensity is obtained through $\log(\text{intensity})$ conversion.

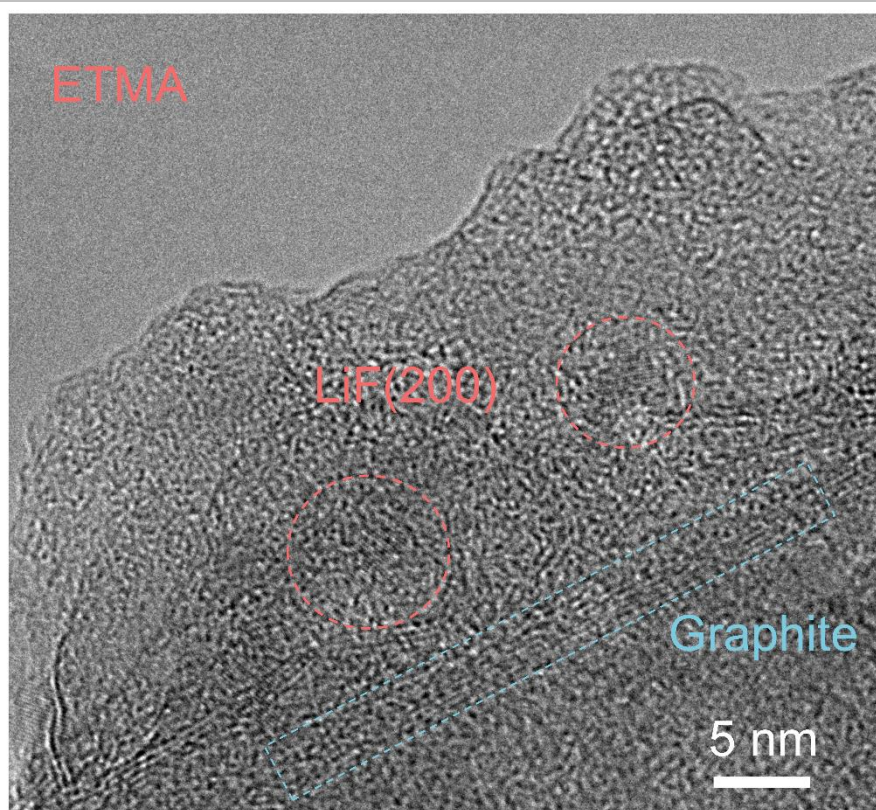


Figure S20. The Cryo-TEM image of graphite anode cycled in ETMA-based electrolyte.

SUPPORTING INFORMATION

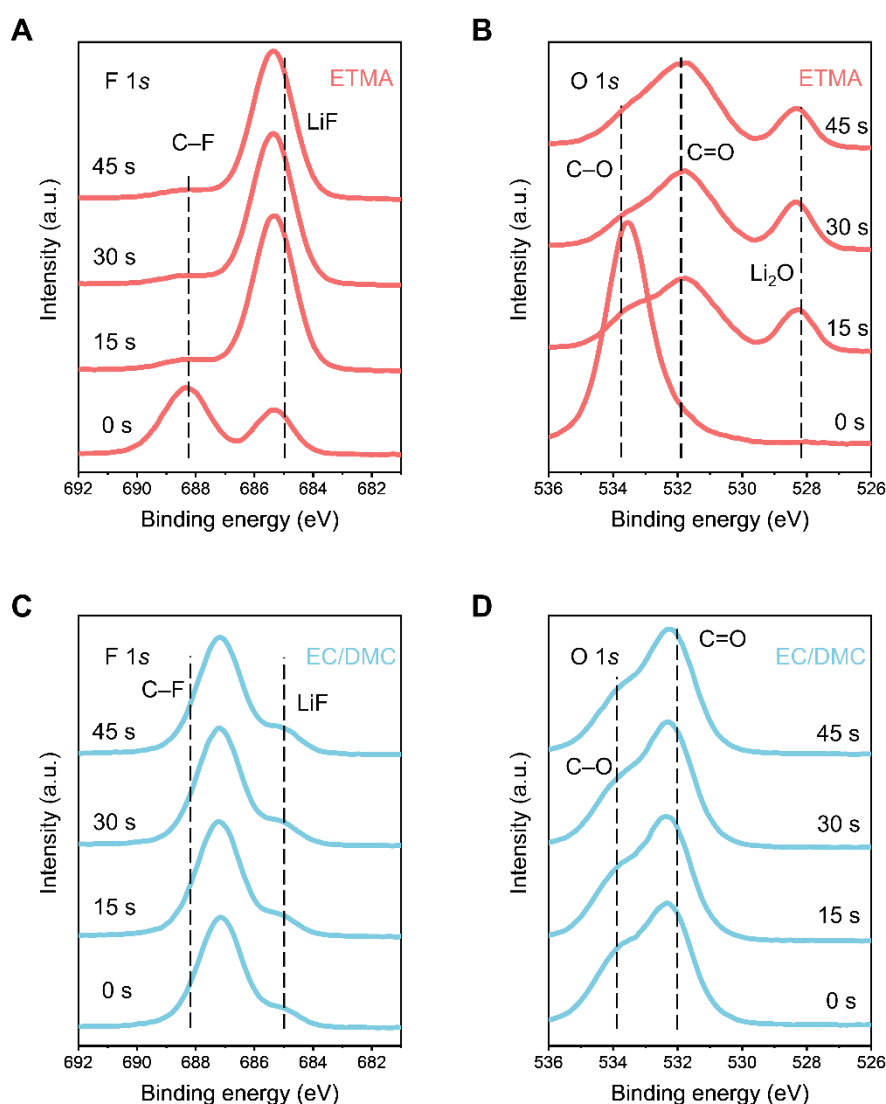


Figure S21. XPS spectra of F 1s and O 1s. (A, C) The F 1s spectra of SEI formed in ETMA- (A) and EC/DMC-based (C) electrolytes, after 0, 15, 30, and 45 s sputtering. (B, D) The O 1s spectra of SEI formed in ETMA- (B) and EC/DMC-based (D) electrolytes, after 0, 15, 30, and 45 s sputtering. The C=O and C–O (the derivatives from organic solvents) signals in XPS O 1s spectra are abundant in the SEI generated in EC/DMC-based electrolyte, while more Li₂O (inorganic components in SEI) signal arises as the sputtering time increasing in the SEI derived from ETMA-based electrolyte, revealing more organic compositions occupy the interfacial film in EC/DMC based electrolyte compared with that in ETMA-based electrolyte.

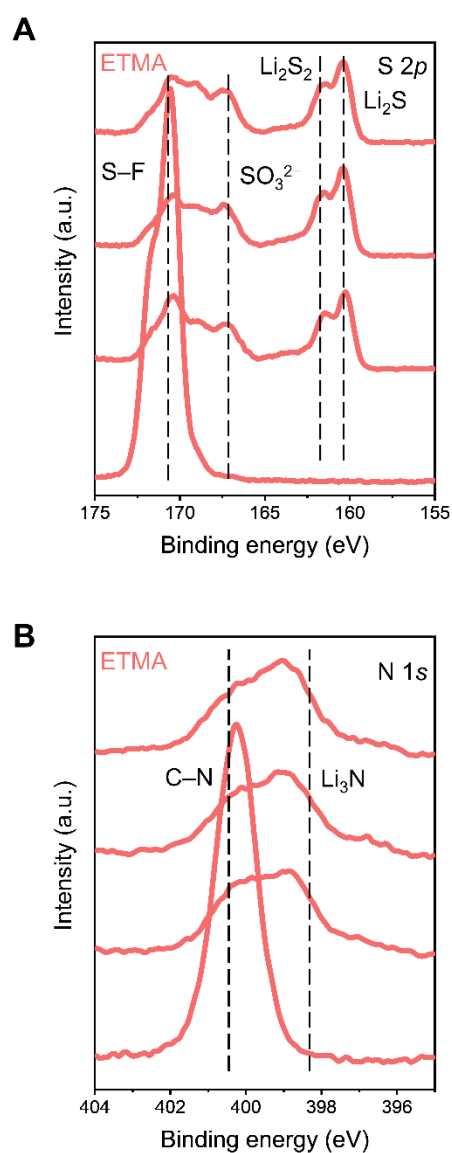


Figure S22. XPS spectra of S 2p and N 1s. (A and B) The S 2p (A) and N 1s (B) spectra of SEI formed in ETMA-based electrolyte after 0, 15, 30, and 45 s sputtering.

SUPPORTING INFORMATION

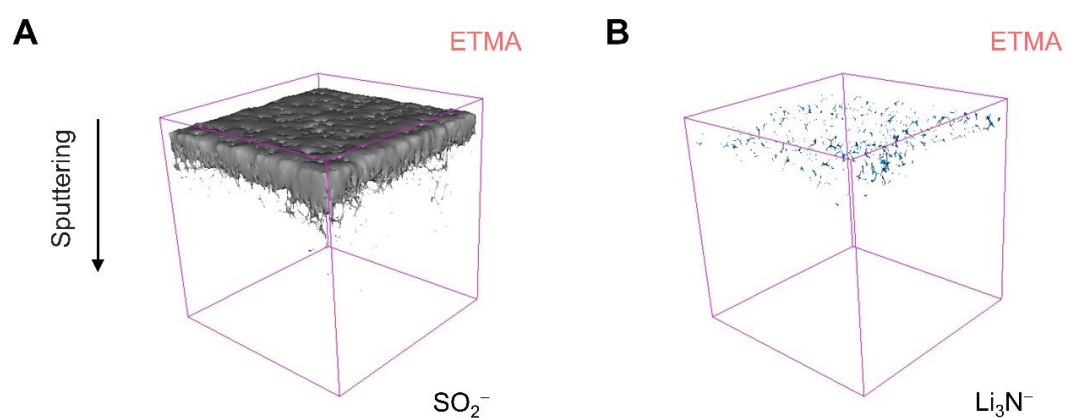


Figure S23. Surface ToF-SIMS components mapping on graphite anodes. (A and B) The SO_2^- (A) and Li_3N^- (B) fragments in the SEI on graphite anodes cycled in ETMA-based electrolytes.

SUPPORTING INFORMATION

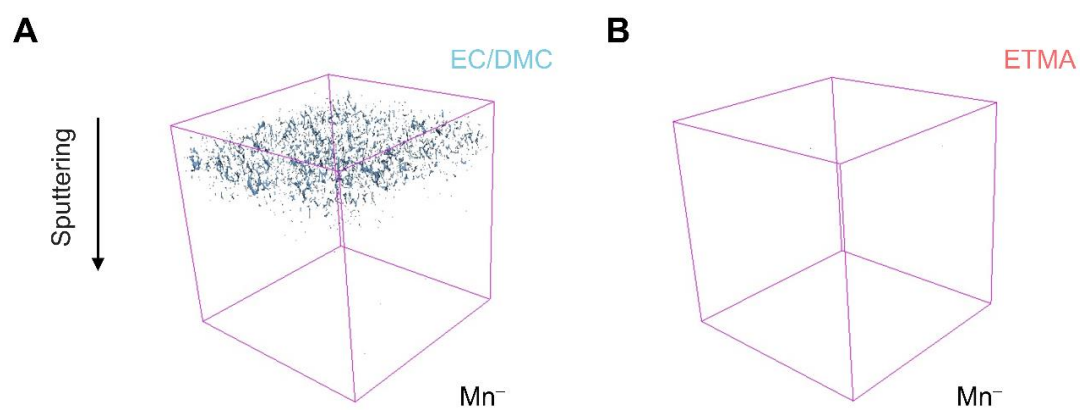


Figure S24. Surface ToF-SIMS components mapping on graphite anodes. (A and B) The Mn^+ fragment in the SEI on graphite anodes cycled in EC/DMC- (A) and ETMA- (B) based electrolytes.

SUPPORTING INFORMATION

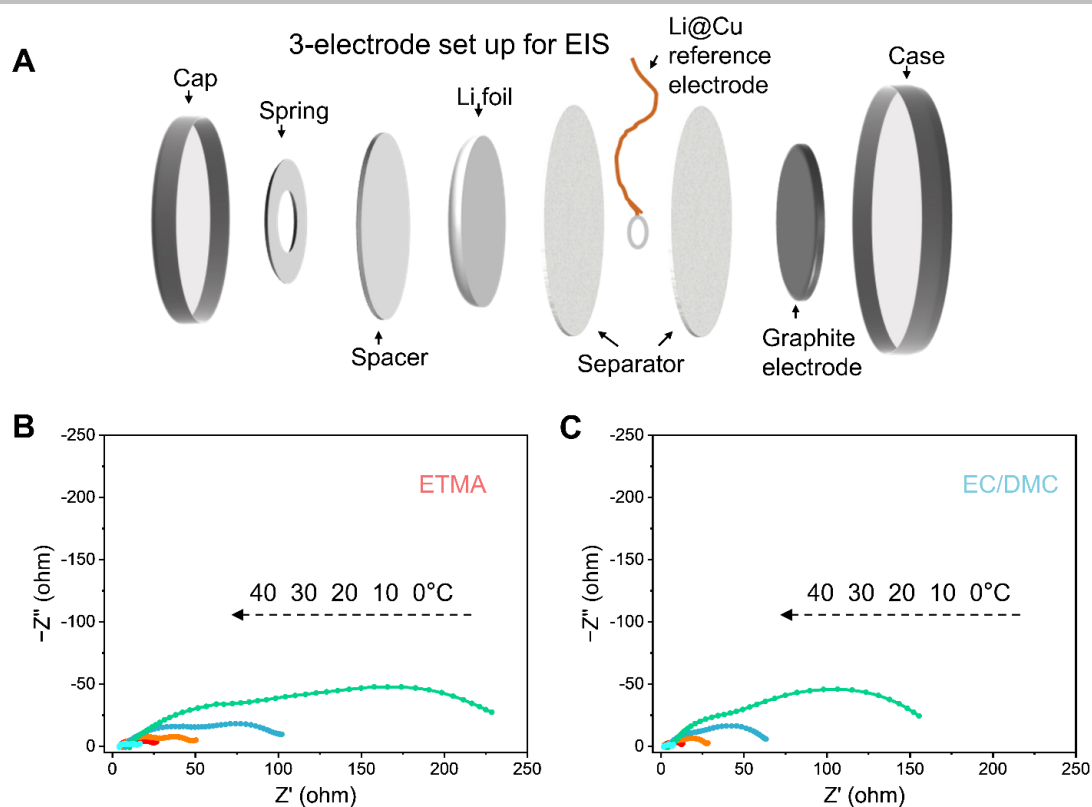


Figure S25. Temperature-dependent EIS spectra based on 3-electrodes. (A) The assembly diagram of 3-electrodes. (B and C) The temperature-dependent EIS spectra of cells with ETMA- (B) and EC/DMC- (C) based electrolytes.

SUPPORTING INFORMATION

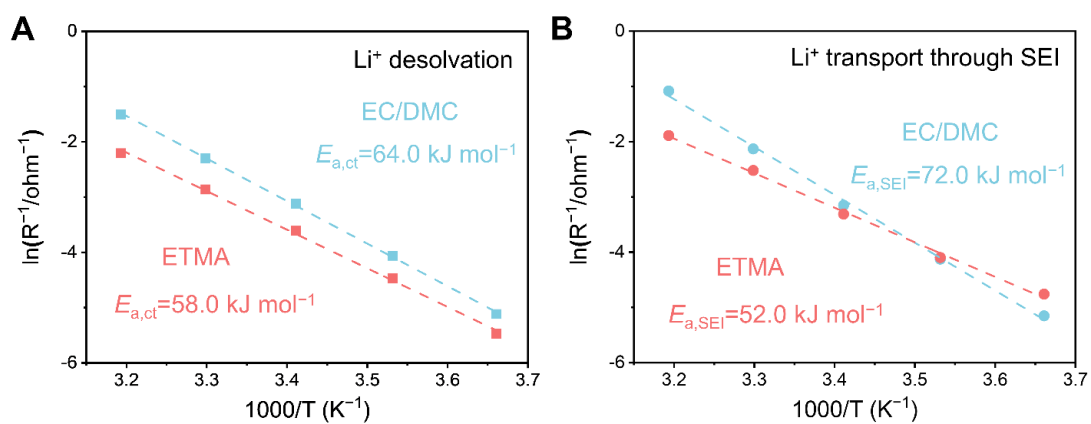


Figure S26. Arrhenius behavior of the resistance corresponding to the desolvation process in two different electrolytes. (A) Arrhenius behavior of the resistance corresponding to Li⁺ desolvation. (B) Arrhenius behavior of the resistance corresponding to Li⁺ transport through SEI.

SUPPORTING INFORMATION

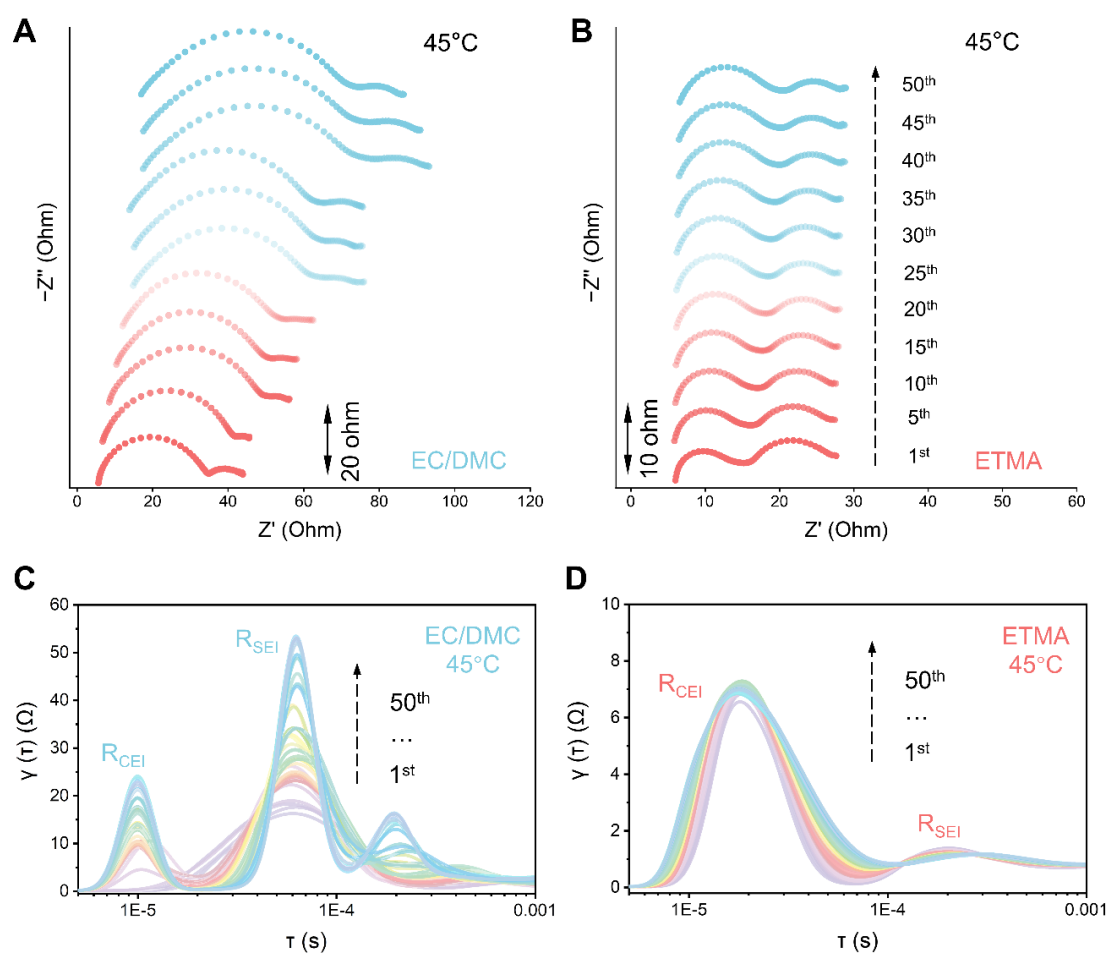


Figure S27. The evolution of interphasial resistance in various electrolytes under 45°C. (A and B) The resistance evolution of full cells using analyzed by EIS in EC/DMC- (A) and ETMA- (B) based electrolytes under 45°C within 50 cycles. (C and D) The evolution of interfacial resistance of graphite||NCM811 full cells analyzed by DRT within 50 cycles, at 45°C in EC/DMC- (C) and ETMA- (D) based electrolytes.

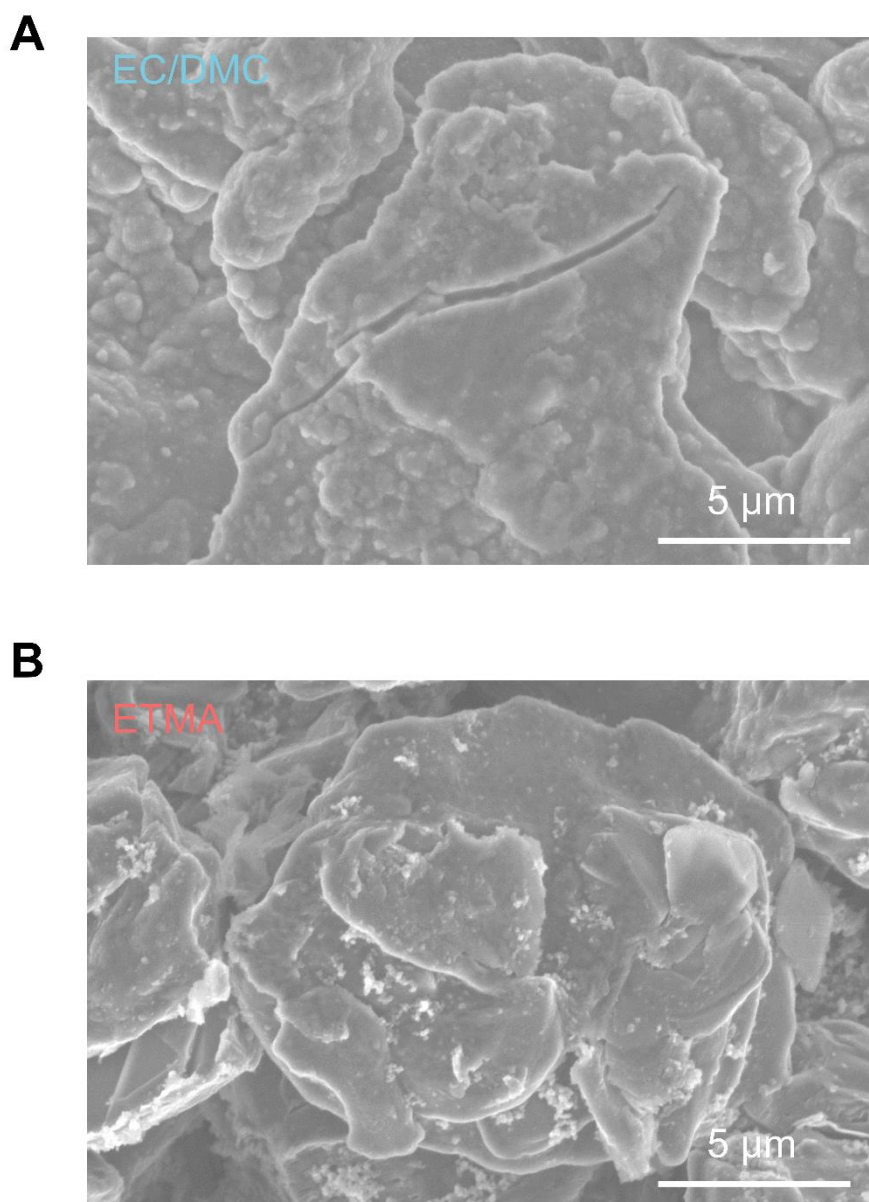


Figure S28. SEM images of graphite anodes after cycled under 45°C. (A and B) The cycled graphite anodes in EC/DMC- (A) and ETMA- (B) based electrolytes.

SUPPORTING INFORMATION

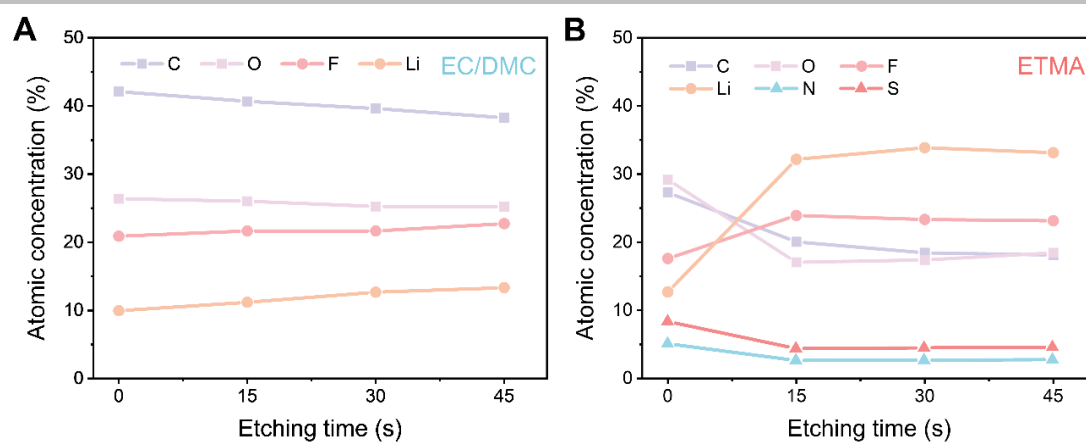


Figure S29. Atomic concentration at different etching times. (A and B) The atomic concentration of SEI formed in (A) EC/DMC- and (B) ETMA-based electrolytes with different sputtering times.

SUPPORTING INFORMATION

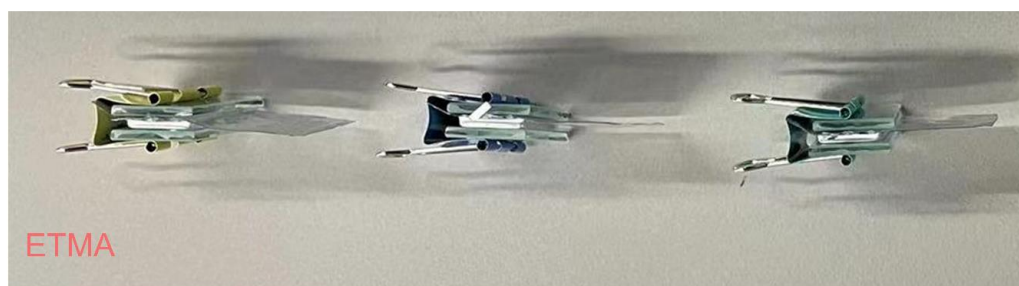
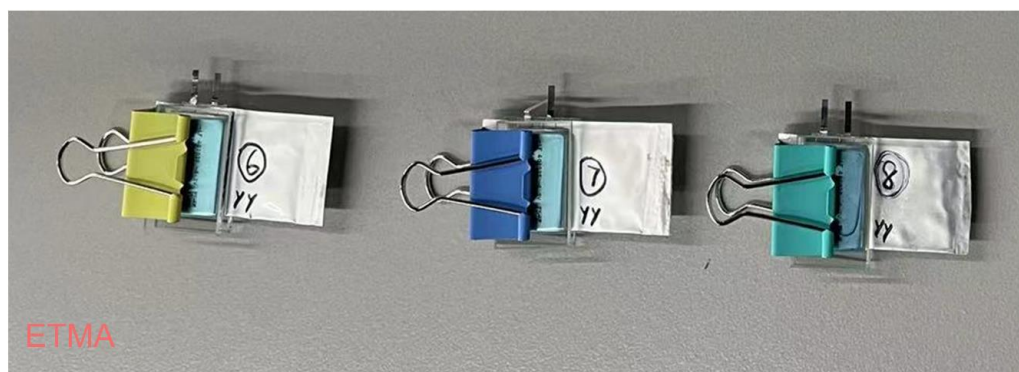
A**B**

Figure S30. The photos of pouch cells after two formation cycles. (A) Side view, (B) Top view. No gas generation in the pouch cells using ETMA-based electrolyte.

SUPPORTING INFORMATION

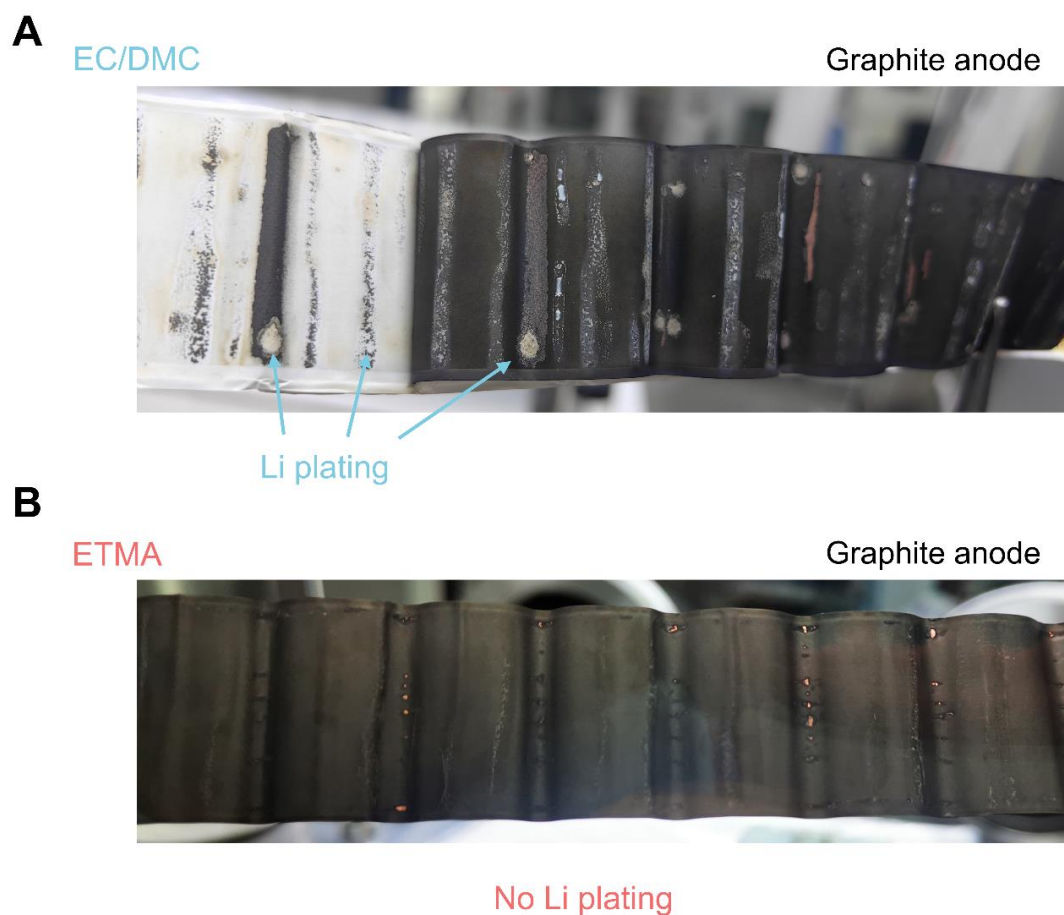


Figure S31. The post-mortem images of cycled graphite anodes. (A) The cycled graphite anodes using EC/DMC-based electrolyte, with severe Li plating. (B) The cycled graphite anodes using ETMA-based electrolyte, without Li plating.

SUPPORTING INFORMATION

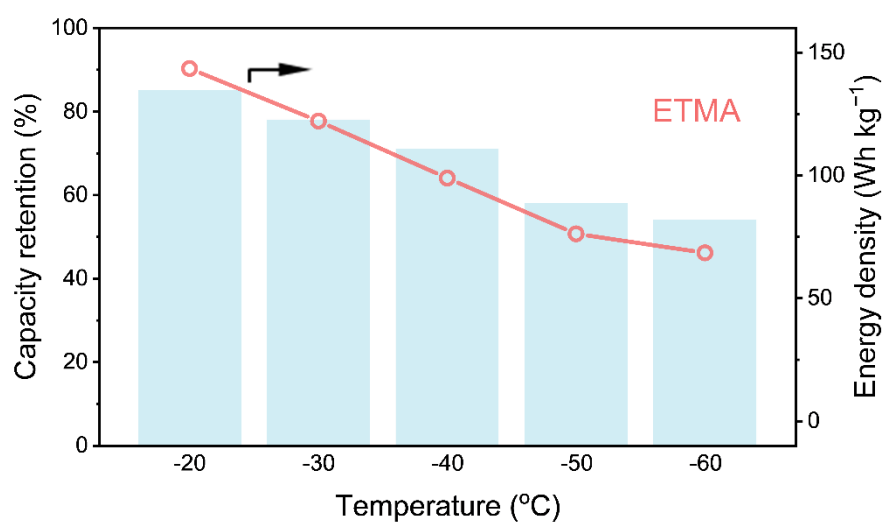


Figure S32. The low-temperature performance of pouch cell using ETMA-based electrolyte, from -20°C to -60°C.

SUPPORTING INFORMATION

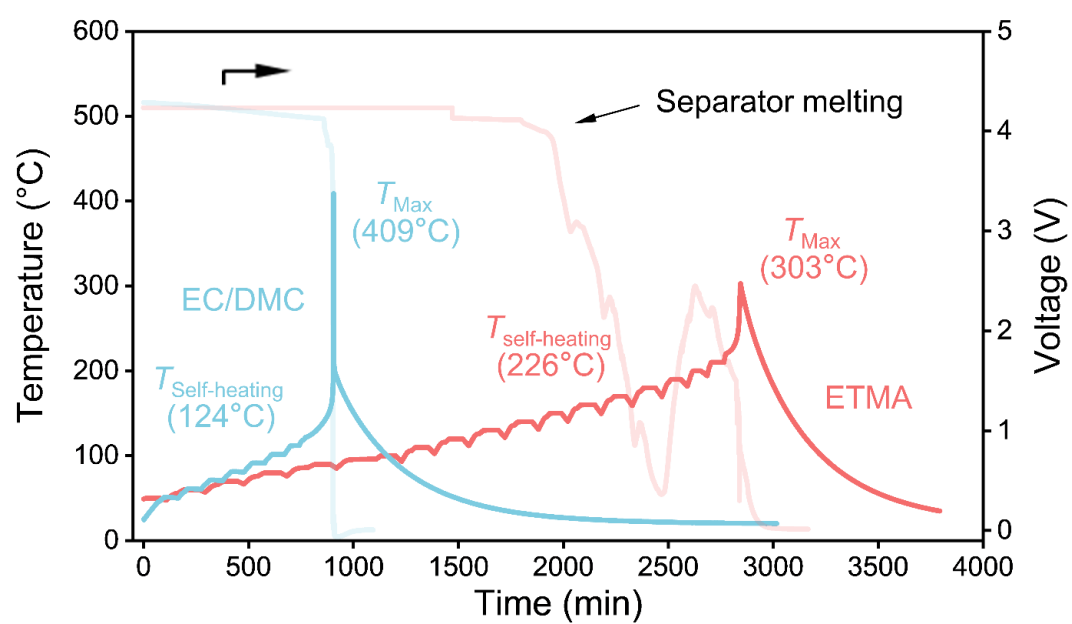


Figure S33. ARC results of pouch cells with different electrolytes with corresponding heating rate and voltage curves.

SUPPORTING INFORMATION

5. References

- [1] B. D. McKay, M. A. Yirik, C. Steinbeck, Surge: a fast open-source chemical graph generator. *J. Cheminformatics* **2022**, *14*, 24.
- [2] M. J. Frisch, G. W. Trucks, H. B. Schlegel, G. E. Scuseria, M. A. Robb, J. R. Cheeseman, G. Scalmani, V. Barone, G. A. Petersson, H. Nakatsuji, X. Li, M. Caricato, A. V. Marenich, J. Bloino, B. G. Janesko, R. Gomperts, B. Mennucci, H. P. Hratchian, J. V. Ortiz, A. F. Izmaylov, J. L. Sonnenberg, Williams, F. Ding, F. Lipparini, F. Egidi, J. Goings, B. Peng, A. Petrone, T. Henderson, D. Ranasinghe, V. G. Zakrzewski, J. Gao, N. Rega, G. Zheng, W. Liang, M. Hada, M. Ehara, K. Toyota, R. Fukuda, J. Hasegawa, M. Ishida, T. Nakajima, Y. Honda, O. Kitao, H. Nakai, T. Vreven, K. Throssell, J. A. Montgomery Jr., J. E. Peralta, F. Ogliaro, M. J. Bearpark, J. J. Heyd, E. N. Brothers, K. N. Kudin, V. N. Staroverov, T. A. Keith, R. Kobayashi, J. Normand, K. Raghavachari, A. P. Rendell, J. C. Burant, S. S. Iyengar, J. Tomasi, M. Cossi, J. M. Millam, M. Klene, C. Adamo, R. Cammi, J. W. Ochterski, R. L. Martin, K. Morokuma, O. Farkas, J. B. Foresman, D. J. Fox, Gaussian Inc., Wallingford, CT, **2016**.
- [3] A. D. Becke, Density-functional thermochemistry. III. The role of exact exchange. *J. Chem. Phys.* **1993**, *98*, 5648–5652.
- [4] P. Steve, Fast parallel algorithms for short-range molecular-dynamics. *J. Comput. Phys.* **1995**, *117*, 1–19.
- [5] W. L. Jorgensen, D. S. Maxwell, J. Tirado-Rives, Development and testing of the OPLS all-atom force field on conformational energetics and properties of organic liquids. *J. Am. Chem. Soc.* **1996**, *118*, 11225–11236.
- [6] G. A. Kaminski, R. A. Friesner, Evaluation and Reparametrization of the OPLS-AA Force Field for Proteins via Comparison with Accurate Quantum Chemical Calculations on Peptides. *J. Phys. Chem. B* **2001**, *105*, 6474–6487.
- [7] L. S. Dodda, I. C. de Vaca, J. Tirado-Rives, W. L. Jorgensen, LigParGen web server: an automatic OPLS-AA parameter generator for organic ligands. *Nucleic Acids Res.* **2017**, *45*, W331–W336.
- [8] A. V. Marenich, S. V. Jerome, C. J. Cramer, D. G. Truhlar, Charge model 5: An extension of hirshfeld population analysis for the accurate description of molecular interactions in gaseous and condensed phases. *J. Chem. Theory Comput.* **2012**, *8*, 527–541.
- [9] J. Z. Vilseck, J. Tirado-Rives, W. L. Jorgensen, Evaluation of CM5 charges for condensed-phase modeling. *J. Chem. Theory Comput.* **2014**, *10*, 2802–2812.
- [10] T. Lu, F.-W. Chen, Multiwfn: a multifunctional wavefunction analyzer. *J. Comput. Chem.* **2012**, *33*, 580–592.
- [11] M. Schauerl, P. S. Nerenberg, H. Jang, L. P. Wang, C. I. Bayly, D. L. Mobley, M. K. Gilson, Non-bonded force field model with advanced restrained electrostatic potential charges (RESP2). *Commun. Chem.* **2020**, *3*, 44.
- [12] K. P. Jensen, W. L. Jorgensen, Halide, ammonium, and alkali metal ion parameters for modeling aqueous solutions. *J. Chem. Theory Comput.* **2006**, *2*, 1499–1509.

SUPPORTING INFORMATION

- [13] J. N. C. Lopes, K. Shimizu, A. A. H. Padua, Y. Umebayashi, S. Fukuda, K. Fujii, S. I. Ishiguro, Potential energy landscape of bis(fluorosulfonyl)amide. *J. Phys. Chem. B* **2008**, *112*, 9449–9455.
- [14] L. Martinez, R. Andrade, E. G. Birgin, J. M. Martinez, PACKMOL: A package for building initial configurations for molecular dynamics simulations. *J. Comput. Chem.* **2009**, *30*, 2157–2164.
- [15] W. G. Hoover, Canonical dynamics: Equilibrium phase-space distributions. *Phys. Rev. A* **1985**, *31*, 1695–1697.
- [16] S. Nose, A molecular dynamics method for simulations in the canonical ensemble. *Mol. Phys.* **1984**, *52*, 255–268.
- [17] M. Parrinello, A. Rahman, Polymorphic transitions in single crystals: A new molecular dynamics method. *J. Appl. Phys.* **1981**, *52*, 7182–7190.
- [18] A. V. Marenich, C. J. Cramer, D. G. Truhlar, Universal solvation model based on solute electron density and on a continuum model of the solvent defined by the bulk dielectric constant and atomic surface tensions. *J. Phys. Chem. B* **2009**, *113*, 6378–6396.
- [19] N. Yao, X. Chen, X. Shen, R. Zhang, Z.-H. Fu, X.-X. Ma, X.-Q. Zhang, B.-Q. Li, Q. Zhang, An Atomic Insight into the Chemical Origin and Variation of the Dielectric Constant in Liquid Electrolytes. *Angew. Chem. Int. Ed.* **2021**, *60*, 21473–21478.
- [20] B. Doherty, X. Zhong, S. Gathiaka, B. Li, O. Acevedo, Revisiting OPLS Force Field Parameters for Ionic Liquid Simulations. *J. Chem. Theory Comput.* **2017**, *13*, 6131–6145.
- [21] G. Z. a. Z. G. a. Q. D. a. H. Z. a. H. X. a. Z. W. a. L. Z. a. G. Ke, in *The Eleventh International Conference on Learning Representations*, **2023**.
- [22] S. Kim, J. Chen, T. Cheng, A. Gindulyte, J. He, S. He, Q. Li, B. A. Shoemaker, P. A. Thiessen, B. Yu, L. Zaslavsky, J. Zhang, E. E. Bolton, PubChem 2023 update. *Nucleic Acids Res.* **2022**, *51*, D1373–D1380.
- [23] H. E. Pence, A. Williams, ChemSpider: An Online Chemical Information Resource. *J. Chem. Educ.* **2010**, *87*, 1123–1124.
- [24] D. Weininger, SMILES, a chemical language and information system. 1. Introduction to methodology and encoding rules. *J. Chem. Inf. Comp. Sci.* **1988**, *28*, 31–36.
- [25] D. Rogers, M. Hahn, Extended-Connectivity Fingerprints. *J. Chem. Inf. Model.* **2010**, *50*, 742–754.
- [26] L. Maaten, G. Hinton, Visualizing Data using t-SNE. *J. Mach. Learn. Res.* **2008**, *9*, 2579–2605.
- [27] F. Pedregosa, G. Varoquaux, A. Gramfort, V. Michel, B. Thirion, O. Grisel, M. Blondel, P. Prettenhofer, R. Weiss, V. Dubourg, J. Vanderplas, A. Passos, D. Cournapeau, M. Brucher, M. Perrot, E. Duchesnay, Scikit-learn: Machine Learning in Python. *J. Mach. Learn. Res.* **2011**, *12*, 2825–2830.
- [28] Y. Mo, G. Liu, J. Chen, X. Zhu, Y. Peng, Y. Wang, C. Wang, X. Dong, Y. Xia, Unraveling the temperature-responsive solvation structure and interfacial chemistry for graphite anodes. *Energy Environ. Sci.* **2024**, *17*, 227–237.

SUPPORTING INFORMATION

- [29] Q. K. Zhang, X. Q. Zhang, J. Wan, N. Yao, T. L. Song, J. Xie, L. P. Hou, M. Y. Zhou, X. Chen, B. Q. Li, R. Wen, H. J. Peng, Q. Zhang, J. Q. Huang, Homogeneous and mechanically stable solid-electrolyte interphase enabled by trioxane-modulated electrolytes for lithium metal batteries. *Nat. Energy* **2023**, 8, 725–735.